Chapter 8

Fractal Nature of the Band-Thickness in the Archean Banded Iron Formation in the Yellowknife Greenstone Belt, Northwest Territories, Canada

Nagayoshi Katsuta, Ichiko Shimizu, Masao Takano, Shin-ichi Kawakami, Herwart Helmstaedt and Mineo Kumazawa

Additional information is available at the end of the chapter

http://dx.doi.org/10.5772/55700

1. Introduction

Banded iron formations (BIFs) are chemically precipitated deposits on the Precambrian sea floor and are characterised by alternations of repeat Fe-rich and Si-rich layers [1]. Temporal variations in the volumes of BIFs are considered to be related to early evolution of the atmosphere, oceans, life and the Earth's interior [2, 3]. In general, BIFs contain various scales of banding. Bands with a thickness of several tens of meters to meters, a thickness of centimetres and a thickness of submillimetre to millimetres are named macrobands, mesobands and microbands, respectively [4]. Some depositions are related to periodic phenomena, such as annual cycles [4], tidal and solar cycles [5–7], and Milankovitch cycles [8, 9] in the Precambrian. On the other hand, quantitative analysis of the banding is limited to Paleoproterozoic Hamersley (Superior-type) BIFs, although BIFs occur within an age range from 3.8 Ga to about 0.7 Ga [10]. Therefore, it is necessary to investigate different BIFs, in terms of both their age and type, clarified by size and lithological facies (i.e., Superior- and Algoma-types) to understand the nature of their banded structures.

In this study, we analysed the banded structures in Archean BIFs using a nondestructive micro-X-ray fluorescence (XRF) imaging technique. This technique has been used recently to determine the distribution of major and trace elements in Quaternary sediments and Phanerozoic sedimentary rocks for characterising the paleoclimatic and paleoenvironmental signals [e.g. 11-15]. It has also been used in the analysis of BIF bandings [16–19]. Sakai *et al*. [16] reported on an XRF imaging analysis conducted on an Antarctic BIF that showed a clear striped structure of alternating Fe-rich and Si-rich layers. Matsunaga *et al*. [17] investigated the influence of

alternation and weathering on the banding in terms of the elemental distribution and the chemical forms, showing that the titanium in the BIF preserved the primary depositional structures and that the chemical states of the iron and manganese present alternated with rhythmic changes in the banding. Fukuda *et al.* [18] revealed that titanium-rich layers in the Hamersley BIF are composed of Ti in silicate and titanium oxide layers and suggested that the oxide phase had precipitated in solution, as well as that the silicate phase had originated from a clastic input of terrigenous origin. Pufahl and Fralik [19] found millimetre-scale chemical grading of Fe, Si, Mn, and Al in the mud lamina of a BIF deposited in Paleoproterozoic shallow water. They suggested that these chemical structures resulted from changes in the Fe^{2+}/Mn^{2+} ratio in the water column, along with changes in the concentration of dissolved O_2, together with the precipitation of inorganic SiO_2 and a rainfall input of terrigenous clay. These previous studies on BIFs using XRF imaging techniques focused on internal structures having mesoband units. However, we are interested in a wider range of patterns in the fluctuations of BIF laminations [20].

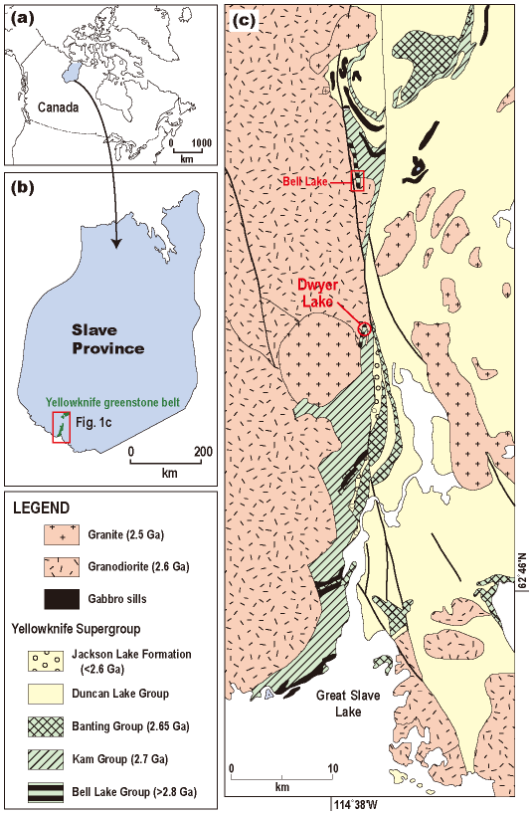

Figure 1. A simplified geological map of the Yellowknife greenstone belt located in the southeastern part of Slave Province, Northwest Territories, Canada, modified from MacLachlan and Helmstaedt [21]. The U–Pb ages are after Isachsen and Bowring [22].

http://dx.doi.org/10.5772/55700

The purpose of this study was to investigate the abundance and variations of the constituent materials in the BIFs, both in the mesobands and on longer spatial scales. In this study, we used an Algoma-type Archean BIF sample with a thickness of about 1.14m, which was collected from a >2.8 Ga Bell Lake Group exposed in the Dwyer Lake area of the Yellowknife greenstone belt, Northwest Territories, Canada (Fig. 1). Based on the results of our XRF imaging analysis and from petrographic observations, we have evaluated whether the banding is a primary or secondary structure, as the constituent materials of the BIF had been completely recrystallized into medium-grade metamorphic minerals under amphibole-facies conditions. After measuring the band-thicknesses of the Fe-rich and Si-rich mesobands using XRF imaging, we investigated the implications of the data for the morphology of the bandings recorded in our BIF samples.

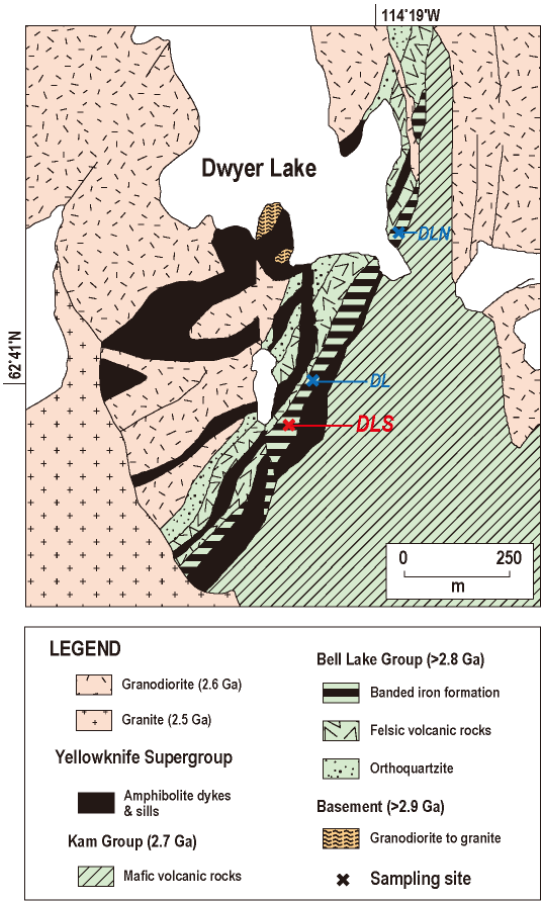

Figure 2. A simplified geological map of the Dwyer Lake area, modified after MacLachlan and Helmstaedt [21]. The U–Pb ages are after Isachsen and Bowring [22]. The sampling points are denoted by the sample names: *DLN*, *DL*, and *DLS*.

2. Samples and methods

2.1. Sampling sites and sample collection

The Yellowknife greenstone belt is the southernmost of approximately 26 granite-greenstone belts in the Slave craton (Fig. 1), and is approximately 35km long and 8–10km wide. The belt is 12km thick, steeply dipping southeast and younging, with homoclinical sequences of calc-alkaline to tholeiitic metavolcanic rocks and metasedimentary rocks [21]. The main volcanic suite of the Yellowknife greenstone belt, composed mainly of tholeiitic pillow lavas, is the Kam Group (ca. 2.7 Ga). The metasedimentary rocks below the granodiorite basement and above the Kam Group (Fig. 2) are divided into the Bell Lake group, which was informally named by Isachsen and Bowring [22]. Here, the term Bell Lake "Group" is used to indicate clearly that it has the rank of a group [20]. The Bell Lake Group is the lowermost part of the Yellowknife Supergroup and comprises orthoquartzite, felsic volcanic rocks and BIF packages from the bottom to the top. In general, the Bell Lake Group is considered to have been formed in a depositional setting, similar to that of a back-arc basin adjacent to a continental margin [21] during transgression [23].

Figure 3. A field photograph of the Dwyer Lake BIF. The light and dark bands on the tabular samples correspond to the Si-rich and Fe-rich mesobands, respectively. The numbers on the sample's surface denote the distance described in intervals of 5cm.

http://dx.doi.org/10.5772/55700

The Bell Lake Group is well-exposed in the Bell Lake and Dwyer Lake areas (Fig. 1). The ages of these regions were determined using U–Pb zircon dates [24]. The felsic volcanic rock below the BIF in the Dwyer Lake region has been dated at 2853 +2/–1 Ma. In the Bell Lake region, the 3m-thick layer of felsic tuff within the 40m-thick BIF unit has an estimated age of 2826 ± 1.5 Ma. In these two regions, we collected continuous BIF tabular samples from the steeply dipped outcrops using a portable diamond cutter (Fig. 3) [14]. In the Bell Lake region, samples from five sequences were taken from the island inside the lake ([20], Fig. 1). On the other hand, in the Dwyer Lake region, the BIF samples were acquired from three sites (*DLN*, *DL*, and *DLS*) that were in close contact with the pillowed volcanic rocks (Fig. 2). The sample taken from *DLN* (62º41′174′′N, 114º18′885′′W) was approximately 112cm long, the sample taken from *DL* (62º40′609′′N, 114º18′740′′W) was approximately 113cm long and the sample taken from *DLS* (62º40′547′′N, 114º18′874′′W) was approximately 114cm long. In the laboratory, the acquired BIF samples were shaped into plates with an area of approximately 20 × 20 cm^2, and a thickness of 3cm for XRF imaging analysis [14]. Hereafter, the sample from the Bell Lake and Dwyer Lake regions will be referred to as the Bell Lake and Dwyer Lake BIF, respectively. In this paper, we present a sequential profile of the *DLS* sample, because the Dwyer Lake BIF samples commonly have a similar pattern of its laminations.

2.2. Analysis

The constituent minerals were identified using an optical microscope, a TOPCON DS-130C scanning electron microscope equipped with a HORIBA EMAX-770X energy dispersive X-ray spectrometer at Nagoya University (Japan) and a microfocused X-ray diffractometer (XRD) (Rigaku PSPC/MDG CN2175-A1) at Nagoya University, equipped with a CrK radiation source (wavelength = 2.2909 Å) and a Cr anode target. The diffraction patterns were matched with data from the Joint Committee on Power Diffraction Standards database [25]. The chemical composition of the amphiboles was analysed using a JEOL JCMA-733 electron-probe micro-analyser at Hokkaido University (Japan), operating at an accelerating voltage of 15kV and a beam current of 20nA. The X-ray intensities were converted to chemical abundances according to the oxide ZAF correction. The concentration of Fe^{2+} and Fe^{3+} was calculated from the total FeO content [26].

We used a HORIBA XGT-2000V scanning X-ray analytical microscope (SXAM) [27] at Nagoya University to extract information from the lamination patterns on the BIF sample surfaces. The high-intensity incident X-rays were emitted from an Rh anode at 50kV and 1mA, focused into a microbeam using an X-ray guide tube with a diameter of 100μm, and irradiated perpendicular to the sample surface. The XRF from the sample surface was analysed using the hi-Si detector of the energy-dispersive spectrometer, and the transmitted X-rays were measured using a NaI scintillation detector. In the SXAM system, the sample was mounted on a motor-driven *X*–*Y* stage and placed in an open space outside the vacuum chamber, so that there was little limitation on the sample size used. A surface area up to 200 × 200mm^2 in size was scanned by the incident X-ray beam, and the XRF intensity data were stored at a resolution of either 256 × 256 pixels or 512 × 512 pixels. In the 512 × 512 pixel mode, seven elements between Na and U, as well as the transmitted X-rays, could be analysed simultaneously. Alternatively, 31

elements, as well as the transmitted X-rays, could be analysed in the 256 × 256 pixel mode. The standard measurement time required to acquire a 512 × 512 pixel image was about 40 hours.

3. Results

3.1. Distribution of the major elements

The major elements in the Dwyer Lake BIF samples detected by our SXAM analysis were Fe, Si, Ca, Mn, K, P, S, and Ti (Fig. 4a). Because the concentration of Ti was relatively low, the first seven elements were selected for SXAM imaging analysis in the 512 × 512 pixel mode. The weight percentage of these seven elements was estimated to be > 95%. The scanning area for the imaging analysis was fixed at 51.2 × 51.2mm^2, and the scan step size was 100μm. The XRF images were acquired allowing overlapping with the adjacent sections above and below to obtain continuous sequence data. The XRF images were reduced to one-dimensional profiles using lamination trace techniques [28] that enabled us to obtain the average value along the deformed bedding planes. After the weighted averages of the overlap sections had been calculated, the sequential profiles shown in Fig. 5a were obtained.

In the XRF images shown in Fig. 4b, the Fe-rich and Si-rich mesobands correspond to the green and white layers shown in the outcrop in Fig. 3, respectively. Fe, Ca, and Mn were enriched in the Fe-rich mesobands, while the Si-rich mesobands contained thin Fe-rich layers (millimetre bands) 0.3–2.0mm thick. Potassium was concentrated locally in the strikingly deformed and altered layers, while phosphorus occurred in thin layers in the Fe-rich mesobands together with Ca. Sulphur was irregularly distributed in both the Fe-rich and Si-rich mesobands. Because K, P, and S occurred in low concentrations and showed no distinct patterns, they are not shown in the XRF images in Fig. 4b.

3.2. Petrology and mineralogy

The Fe-rich mesobands were composed of actinolite, magnetite, quartz, and trace amounts of apatite and pyrite (Fig. 6a). The Si-rich mesobands were composed of quartz, magnetite and trace actinolite. The nomenclature used for the amphiboles follows Leake *et al.* [29]. The Fe-rich mesobands corresponded to the layers shown in the XRF maps of Fe, Ca, and Mn.

Magnetite grains in the Fe-rich mesobands formed several hundred μm-thick layers (Fig. 6a). The Si-rich mesobands were composed of quartz and magnetite, with minor actinolite (Fig. 6b), which correspond to the layers shown in the Si map. The constituent minerals in the

Dwyer Lake BIF samples correspond to the medium- to high-grade metamorphic zones described by Klein [10]. Magnetite grains in the Si-rich mesobands were either included in the quartz matrix or arranged as microbands (Fig. 6b).

The actinolite in the Fe-rich mesobands was green in colour and was either euhedral or subhedral (Fig. 6a). The dimensions of the actinolite were typically approximately 100μm in the direction of the crystallographic *c*-axis and <50μm in the direction perpendicular to the *c*-

http://dx.doi.org/10.5772/55700

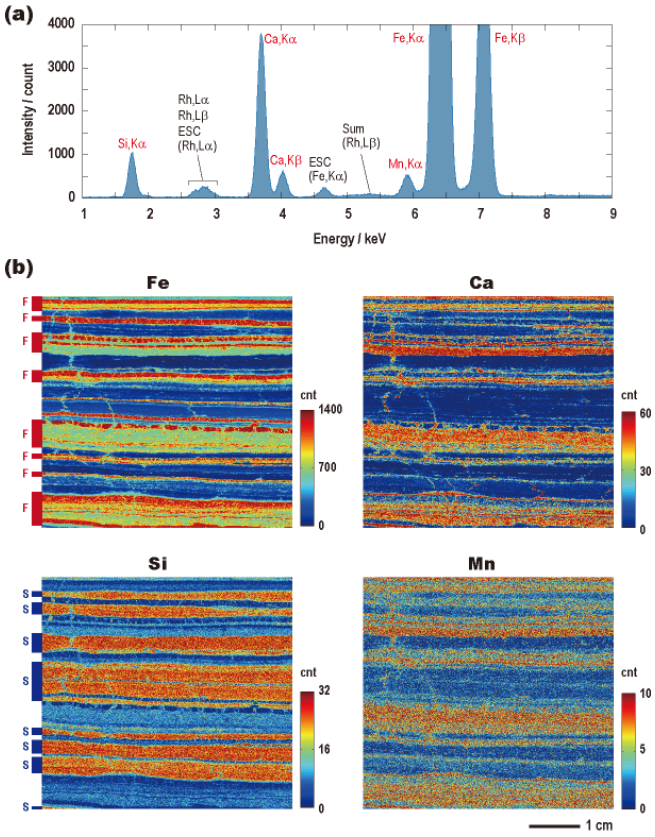

Figure 4. Micro-XRF analysis of a BIF sample (*DLS* 35–45). (a) Cumulative energy spectrum captured using SXAM for an Fe-rich mesoband. The terms ESC and SUM denote the escape and the sum peak, respectively. The Rh peaks denote signals from the Rh target. (b) XRF images of a BIF sample. Key: F = Fe-rich mesoband, and S = Si-rich mesoband. The size of the digitised images represents 512 × 512 pixels. The step size in the *x*–*y* scan is 100μm. The XRF intensity is represented by the X-ray photon count (cnt).

axis. The actinolite lacked any exsolution textures. Actinolite also occurred locally in the quartz matrix of the Si-rich mesobands. The magnetite grains in Fe-rich mesobands and in microbands within the Si-rich mesobands were relatively large (length = approximately 100μm), and were mostly oblate. Outside the Fe-rich mesobands and microbands, magnetite occurred in small grains included within polygonal quartz grains or at the boundaries of quartz grains. The quartz showed an undulatory extinction.

The schistosity was determined from the preferred orientation of the actinolite grains in the Fe-rich mesobands and in the quartz matrix, and by the preferred orientation of the oblate magnetite. The schistosity was subparallel to the banded structures in the Dwyer Lake BIF samples.

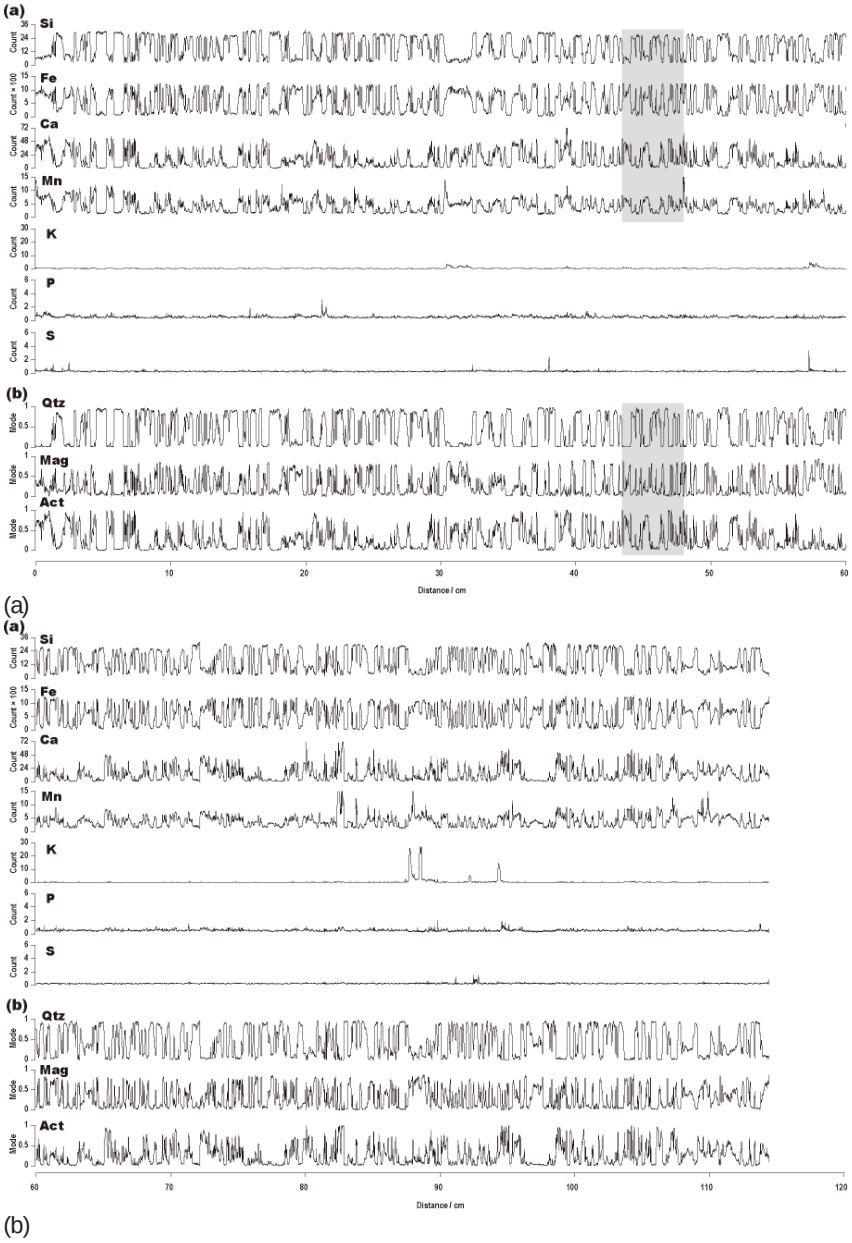

Figure 5. Chemical profiles of the Dwyer Lake BIF samples (*DLS*) in the direction orientated perpendicular to the banded structures. (a) Elemental profiles. The relative abundance of Si, Fe, Ca, Mn, K, P and S are represented by the X-ray photon counts acquired during the micro-XRF analysis. (b) Mineral profiles are calculated from the XRF intensity for Si, Fe, Ca, and Mn. The shaded area corresponds to the XRF images in Fig. 4 and the mineral mode profiles shown in Fig. 7. The abbreviations of the mineral phases follow Kretz [35].

http://dx.doi.org/10.5772/55700

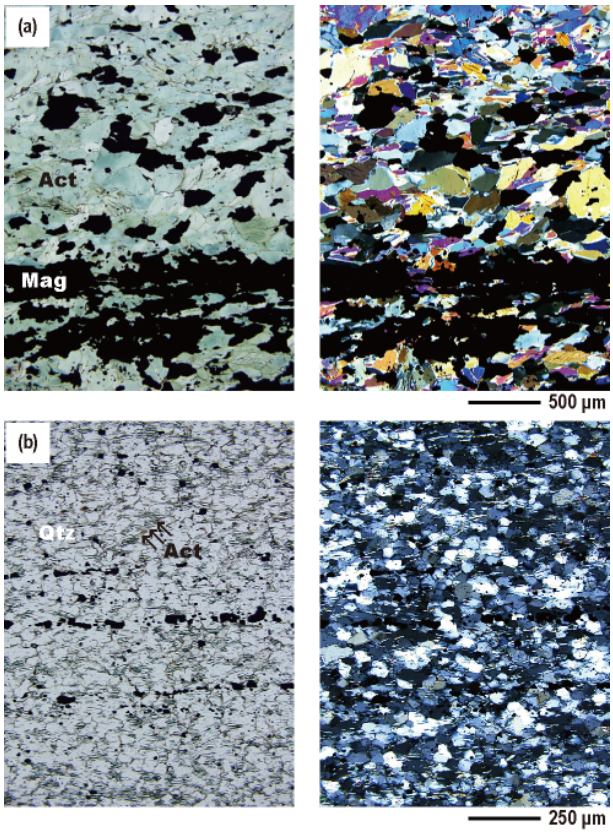

Figure 6. Photomicrographs of BIF sections (*DLN*) cut normally to the banded structures. Left: plane-polarised light. Right: crossed-polarised light. (a) Fe-rich mesoband and (b) Si-rich mesoband.

3.3. Modal compositions

The measured XRF intensity in the element images for a given pixel is related to the bulk concentration of the elements of the constituent mineral for that pixel. Therefore, we assumed that the XRF intensity was linearly proportional to the volume proportion in the mineral, and therefore determined the modal proportions of the constituent minerals in the Dwyer Lake BIF samples (Figs 5b and 7) using the algorithm of Togami *et al*. [30]. The minor minerals were ignored in our calculations and we approximated the samples as being a mixture of three minerals: quartz, magnetite and actinolite. The modal proportions of these three minerals were determined from the XRF intensity profiles of Si, Fe, Ca, and Mn (Fig. 5a). The minor phases of apatite and pyrite were estimated to be <1%. Details of the computation methods are described in Katsuta *et al*. [20].

The modal proportion of actinolite was typically 0.6–1.0 in the Fe-rich mesobands, and <0.2 in the Si-rich mesobands. The modal proportion of magnetite was 0.3–0.8 in the Fe-rich meso-

bands and approximately 0.7 in the Si-rich mesobands. The magnetite peaks shown in Fig. 7 correspond to a high Fe content in the XRF map (Fig. 4b). The distributions of Ca and Mn in the XRF maps show high concentrations of actinolite. The relationship between actinolite and magnetite in the Fe-rich mesobands and that between magnetite and quartz in the Si-rich mesobands show an inverse correlation.

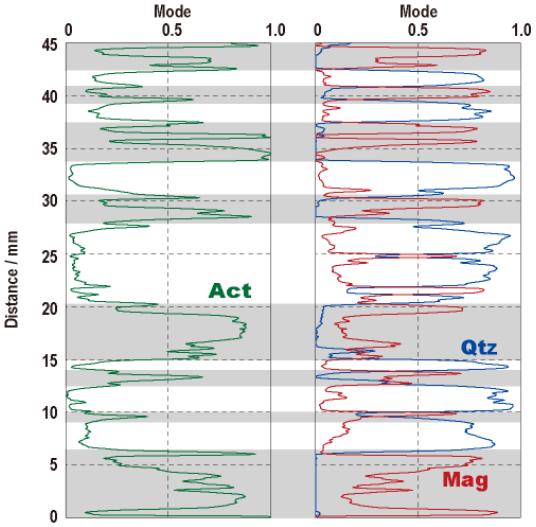

Figure 7. Mineral mode profiles corresponding to the XRF images shown in Fig. 5. The shaded and white bands indicate Fe-rich and Si-rich mesobands, respectively.

3.4. Band-thicknesses

The thickness of the Fe-rich and Si-rich mesobands was analysed using the element and mineral profiles (Figs 5 and 7). The results of our analysis are shown in Fig. 8. The Fe-rich mesobands had a thickness range of 0.1 to 1.4cm (average = 0.35cm) and the Si-rich mesobands had a thickness range of 0.1 to 1.1cm (average = 0.25cm). A thickness of approximately 0.1cm was the cutoff scale for these two mesobands. The number of these mesobands that could be identified was 190 over the entire *DLS* sequence (114cm in length). The frequency distribution showed an exponential decrease in the number of thicker bands.

4. Discussion

4.1. Influence of metamorphism on banded structures

The Dwyer Lake BIF suffered amphibole-facies metamorphism and the constituent minerals were completely recrystallized into medium-grade metamorphic minerals (Fig. 6). The

http://dx.doi.org/10.5772/55700

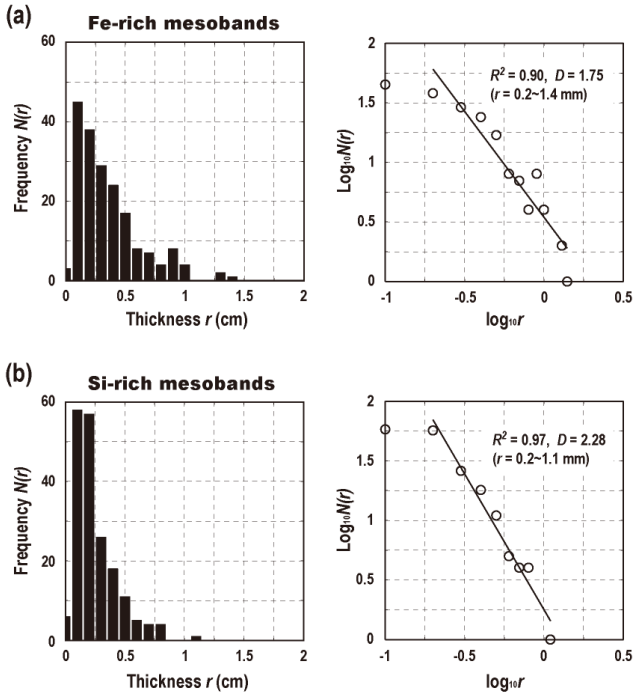

Figure 8. Frequency distributions of the band-thicknesses of the Dwyer Lake BIF samples (*DLS*). Left: a linear scale. Right: a logarithmic scale. (a) Fe-rich mesobands. (b) Si-rich mesobands. *R*: correlation coefficient. *D*: fractal dimension.

schistosity defined by the preferred orientation of elongated actinolite and magnetite was approximately parallel to the boundary between the Fe-rich and Si-rich mesobands. Because of this, it was difficult to evaluate whether the bandings were primary sedimentary structures or secondary metamorphic layers.

In a previous study, we investigated the banded structures in Bell Lake BIF samples [20], which have the same stratigraphic position (Bell Lake Group) as the Dwyer Lake BIF samples (Fig. 1). The Bell Lake BIF had metamorphosed to amphibolites facies and had the schistosity subparallel to the banded structures, as the Dwyer Lake BIF had. Meanwhile, in the Bell Lake BIF samples, we found that the schistosity clearly intersected the boundary between the Fe-rich and Si-rich mesobands in a locally developed intrafolial fold. This implies that the alternating structures of the Fe-rich and Si-rich mesobands already existed at the time of peak metamorphism.

In the Bell Lake BIF samples, the Fe-rich mesobands were mainly composed of hornblende, grunerite, and magnetite. The hornblende was concentrated in the middle part of the Fe-rich mesobands, and was sandwiched between grunerite layers at the margins of the Fe-rich mesoband, which suggests that metamorphic differentiation occurred in the Fe-rich meso-

bands. The mineral phases and petrographic textures are markedly different from those in the Dwyer Lake BIF samples.

The differences between the Bell Lake and Dwyer Lake BIF samples could have arisen from different initial bulk compositions and perhaps from different metamorphic temperatures. It has been suggested that the Bell Lake BIF had possibly been subjected to a stronger influence of metamorphism compared with the Dwyer Lake BIF. Therefore, we regard the banding and band-thickness of the Dwyer Lake BIF to be a primary sedimentary structure. As has been discussed for the Bell Lake BIF [20], the source of the constituent materials in the Fe-rich mesobands was interpreted as being from mafic pyroclastic materials arising from submarine volcanic eruptions, given that the Bell Lake Group was formed at a time of continental breakup and rifting.

4.2. Causes of the banding in the Dwyer Lake BIF

As shown in Fig. 8, the frequency distribution of the band-thickness in the Fe-rich and Si-rich mesobands in the Dwyer Lake BIF shows an exponential decrease in the number of thicker bands. This suggests that the band-thickness follows a power law distribution. Hence, we determined the scaling exponent, D, of the band-thickness, r, (above the 0.1cm cutoff scale) using the equation

$$N(r) = a \cdot r^{-D}, \tag{1}$$

where N is the number of bands and a is a constant. Consequently, the value of D for the Fe-rich mesobands was 1.75 with a correlation coefficient of $R = -0.95$ and the value of D for the Si-rich mesobands was 2.28 where $R = -0.98$. This statistically significant result implies that the Fe-rich and Si-rich mesobands have a fractal nature.

It is well known that the BIFs have hierarchical structures comprising macrobands (meters thick), mesobands (centimetres thick), and microbands (millimetres thick) [4]. On the other hand, evidence that BIFs have fractal dimensions of the band-thickness, i.e., D, has also been observed in the Archean BIF, Kola Peninsula, Russia [31]. Goryainov *et al.* [31] reported that the magnetite bands had a thickness distribution of $D = 1.74 \pm 0.1$. This is comparable to that of Fe-rich mesobands in the Dwyer Lake BIF ($D = 1.75$).

In the Dwyer Lake BIF, the most striking feature is that not only the Fe-rich mesobands but also the paired Si-rich mesobands exhibit a fractal nature. In general, it is believed that the absence of silica-secreting organisms in the Precambrian seawater may have led to it be saturated with respect to dissolved silica and the silica was maintained at a saturated level throughout periods of both high and low iron supply [32]. If this model is applied to the bandings in the Dwyer Lake BIF, then the thickness and spacing of the Fe-rich mesobands could be interpreted as indicating deposition by a nonstochastic process.

To our knowledge, the geological evidence that bed thickness follows a power law is limited to observations on turbidite sequences [33] and biocalcarenitic tidal dune successions [34].

http://dx.doi.org/10.5772/55700

However, such depositional processes are different from those of the Fe-rich mesobands in the Dwyer Lake BIF. This is because the constituent materials of the successions are clastic sediments that were supplied from a continental shelf by turbidity currents and deposited in a shelf embayment dominated by tidal currents. Accordingly, we must assign another cause for the morphology of the bandings preserved in the Dwyer Lake BIF.

Presently, we consider the hypothesis of Morris [32] to be the most suitable depositional model for explaining the fractal nature of the Dwyer Lake BIF. It is well known that the banding of mesoband types is well developed in the Hamersley BIF of Western Australia. According to Morris [32], the Fe-rich mesobands resulted from the periodic convection-driven upwelling of pyroclastic materials from a mid-ocean ridge (MOR) or hot spot. Moreover, Morris concluded that the different mesoband types that are intermediate in scale between mesobanding and microbanding were produced by a modified deep-water supply because of varied MOR activity or partial blocking of upwelling water. In the Dwyer Lake BIF, we consider that such an irregular supply of deep seawater may have resulted in the formation of the fractal-like bandings. In addition, the difference in the bandings between the Dwyer Lake and Bell Lake BIFs that have a fractal-like and hierarchical structure [20], respectively, could be explained by the hypothesis of Morris [32].

5. Conclusions

We have investigated the bandings in Archean metamorphic BIF samples collected from the Dwyer Lake area in the Yellowknife greenstone belt, Canada. Chemical and petrographic analysis revealed the following.

1. The Fe-rich and Si-rich mesobands in the Dwyer Lake BIF are regarded as being primary structures formed before metamorphic alternation, based on a comparison with Bell Lake BIF samples.
2. The band-thickness of both the Fe-rich and Si-rich mesobands showed a power law distribution, suggesting a fractal-like nature.
3. The thickness and spacing of the Fe-rich mesobands could have been created by an irregular upwelling of submarine pyroclastic materials.

Acknowledgements

We express our cordial thanks to John A. Brophy and Bill Padgham, Northwest Territories Geoscience Office, for their support in our research activities in Canada. We thank S. Hori, T. Okaniwa, H. Yoshioka, A. Yoshihara, S. Ito, and Y. Isozaki for collecting the BIF samples; S. Yogo for preparing the thin sections; and T. Goto for technical advice on the SEM-EDS analysis. This study was supported by the Decoding Earth Evolution Program (DEEP) Grant-in-Aid for Scientific Research on Priority Areas (No. 07238104); a Grant-in-Aid for Scientific Research for

Young Scientists (B) (No. 19740319, 24700947); Dynamics of the Sun-Earth-Life Interactive System, Number G-4, the 21st Century COE Program for the Ministry of Education, Culture, Sports, Science and Technology, Japan; the Saijiro Endo Memorial Foundation; and the Fujiwara Natural History Foundation.

Author details

Nagayoshi Katsuta[1], Ichiko Shimizu[2], Masao Takano[3], Shin-ichi Kawakami[1], Herwart Helmstaedt[4] and Mineo Kumazawa[3]

1 Faculty of Education, Gifu University, Japan

2 Department of Earth and Planetary Science, Graduate School of Science, University of Tokyo, Japan

3 Graduate School of Environmental Studies, Nagoya University, Japan

4 Department of Geological Science, Queen's University, Canada

References

[1] James HL. Sedimentary facies of iron-formation. Economic Geology 1954;49(3) 235–293.

[2] Klein C, Beukes NJ. Time distribution, stratigraphy, and sedimentologic setting, and geochemistry of Precambrian iron-formations. In: Shopf JW, Klein C. (ed.) The Proterozoic Biosphere: A Multidisciplinary Study. New York: Cambridge University Press; 1992. p139–146.

[3] Isley AE, Abbott DH. Plume-related mafic volcanism and the deposition of banded iron formation. Journal of Geophysical Research 1999;104 (B7) 15461–15477.

[4] Trendall AF, Blockley JG. The iron formations of the Precambrian Hamersley Group, Western Australia. Geological Survey of Western Australia Bulletin 1970;119 1–366.

[5] Trendall AF. Varve cycles in the Weeli Wolli Formation of the Precambrian Hamersley Group, Western Australia. Economic Geology 1973;68(7) 1089–1097.

[6] Walker JCG, Zahnle KJ. Lunar nodal tide and distance to the Moon during the Precambrian. Nature 1986;320(6063) 600–602.

[7] Williams GE. Geological constraints on the Precambrian history of Earth's rotation and the Moon's orbit. Reviews of Geophysics 2000;38(1) 37–59.

[8] Simonson BM, Hassler SW. Was the deposition of large Precambrian iron formations linked to major marine transgressions? Journal of Geology 1996;104(6) 665–675.

[9] Pickard AL, Barley ME, Krapež B. Deep-marine depositional setting of banded iron formation: sedimentological evidence from interbedded clastic sedimentary rocks in the early Palaeoproterozoic Dales Gorge Member of Western Australia. Sedimentary Geology 2004;170(1–2) 37–62.

[10] Klein C. Some Precambrian banded iron-formations (BIFs) from around the world: Their age, geologic setting, mineralogy, metamorphism, geochemistry, and origin. American Mineralogist 2005;90(10) 1473–1499.

[11] Böning P, Bard E, Rose J. Toward direct, micron-scale XRF elemental maps and quantitative profiles of wet marine sediments. Geochemistry Geophysics Geosystem 2007;8(5): Q05004.

[12] Katsuta N, Takano M, Kawakami SI, Togami S, Fukusawa H, Kumazawa M, et al. Climate system transition from glacial to interglacial state around the beginning of the last termination: Evidence from a centennial- to millennial-scale climate rhythm. Geochemistry Geophysics Geosystem 2006;7(12): Q12006.

[13] Katsuta N, Takano M, Kawakami SI, Togami S, Fukusawa H, Kumazawa M, et al. Advanced micro-XRF method to separate sedimentary rhythms and event layers in sediments: its application to lacustrine sediment from Lake Suigetsu, Japan. Journal of Paleolimnology 2007;37(2) 259–271.

[14] Katsuta N, Tojo B, Takano M, Yoshioka H, Kawakami S, Ohno T, et al. Non-destructive method to detect the cycle of lamination in sedimentary rocks: rhythmite sequence in Neoproterozoic cap carbonate. In: Vickers-Rich P, Komarower P. (ed.) The Rise and Fall of the Ediacaran Biota. Geological Society, London, Special Publication. Bath: The Geological Society Publishing House; 2007. p27-34.

[15] Kuroda J, Ohkouchi N, Ishii T, Tokuyama H, Taira A. Lamina-scale analysis of sedimentary components in Cretaceous black shales by chemical compositional mapping: Implications for paleoenvironmental changes during the Oceanic Anoxic Events. Geochimica et Cosmochimica Acta 2005;69(6) 1479–1494.

[16] Sakai H, Shirai K, Takano M, Horii M, Funaki, M. Analysis of fine structure of chert and BIF by measurement of high resolution magnetic field and scanning X-ray analyzed microscope. Proceedings of the NIPR symposium on Antarctic Geosciences 1997;10 59–67.

[17] Matsunaga M, Fukuda K, Kato Y, Nakai I. Characterization of banded iron formations by two-dimensional XRF imaging and XANES analyses. Resource Geology 2000;50(1) 75–81.

[18] Fukuda K, Matsunaga M, Kato Y, Nakai I. Chemical speciation of trace titanium in Hamersley banded iron formations by X-ray fluorescence imaging and XANES analysis. Journal of Trace and Microprobe Techniques 2001;19(4) 509–519.

[19] Pufahl PK, Fralick PW. Depositional controls on Palaeoproterozoic iron formation accumulation, Gogebic Range, Lake Superior region, USA. Sedimentology 2004;51(4) 791–808.

[20] Katsuta N, Shimizu I, Helmstaedt HH, Takano M, Kawakami S, Kumazawa M. Major element distribution in Archean banded iron-formation (BIF): Influence of metamorphic differentiation. Journal of Metamorphic Geology 2012;30(5) 457–472.

[21] MacLachlan K, Helmstaedt H. Geology and geochemistry of an Archean mafic dike complex in the Chan Formation: basis for a revised plate–tectonic model of the Yellowknife greenstone belt. Canadian Journal of Earth Sciences 1995;32(5) 615–630.

[22] Isachsen CE, Bowring SA. The Bell Lake group and Anton Complex: a basement–cover sequence beneath the Archean Yellowknife greenstone belt revealed and implicated in greenstone belt formation. Canadian Journal of Earth Sciences 1997;34(2) 169–189.

[23] Mueller WU, Corcoran PL, Pickett C. Mesoarchean continental breakup: evolution and inferences from the >2.8 Ga Slave craton–cover succession, Canada. Journal of Geology 2005;113(1) 23–45.

[24] Ketchum J, Bleeker W. New field and U-Pb data from the Central Slave Cover Group near Yellowknife and the Central Slave Basement Complex at Point Lake. In: Cook F, Erdmer P. (ed.) Slave-Northern Cordillera Lithospheric Evolution (SNORCLE) Transect and Cordilleran Tectonic Workshop Meeting, February 25–27, 2000, University of Calgary, Canada. Lithoprobe Report 72;2000. p27–31.

[25] Joint Committee on Power Diffraction Standards. Mineral Powder Diffraction File Data Book: Sets 1–50. International Centre for Diffraction Data 2001.

[26] Droop GTR. A general equation for estimating Fe3+ concentrations in ferromagnesian silicates and oxides from microprobe analysis, using stoichiometric criteria. Mineralogical Magazine 1987;51(361) 431–435.

[27] Hosokawa Y, Ozawa S, Nakazawa H, Nakayama Y. An x-ray guide tube and a desktop scanning x-ray analytical microscope. X-Ray Spectrometry 1997;26(6) 380–387.

[28] Katsuta N, Takano M, Okaniwa T, Kumazawa M. Image processing to extract sequential profiles with high spatial resolution from the 2D map of deformed laminated patterns. Computers & Geosciences 2003;29(6) 725–740.

[29] Leake BE, Woolley AR, Arps CES, Birch WD, Gilbert MC, Grice JD, et al. Nomenclature of amphiboles; report of the Subcommittee on Amphiboles of the International Mineralogical Association Commission on New Minerals and Mineral Names. European Journal of Mineralogy 1997;9(3) 623–651.

http://dx.doi.org/10.5772/55700

[30] Togami S, Takano M, Kumazawa M, Michibayashi K. An algorithm for the transformation of XRF images into mineral-distribution maps. Canadian Mineralogist 2000;38(5) 1283–1294.

[31] Goryainov PM, Ivanyuk GYu, Sharov NV. Fractal analysis of seismic and geological data. Tectonophysics 1997;269(3–4) 247–257.

[32] Morris RC. Genetic modelling for banded iron-formation of the Hamersley Group, Pilbara Craton, Western Australia. Precambrian Research 1993;60(1–4) 243–286.

[33] Rothman DH, Grotzinger JP, Flemings P. Scaling in turbidite deposition. Journal of Sedimentary Research 1994;A64(1) 59–67.

[34] Longhitano SG, Nemec W. Statistical analysis of bed-thickness variation in a Tortonian succession of biocalcarenitic tidal dunes, Amantea Basin, Calabria, southern Italy. Sedimentary Geology 2005;179(3–4) 195–224.

[35] Kretz R. Symbols for rock-forming minerals. American Mineralogist 1983;68(1-2) 277–279.